Inorganic Chemistry

Article

pubs.acs.org/IC

Structural, Magnetic, and Electronic Properties of Phenolic Oxime Complexes of Cu and Ni

Alexander M. Whyte,[†] Benjamin Roach,[†] David K. Henderson,[†] Peter A. Tasker,[†] Michio M. Matsushita,[‡] Kunio Awaga,[‡] Fraser J. White,[†] Patricia Richardson,[†] and Neil Robertson*,[†]

[†]School of Chemistry and EaStChem, University of Edinburgh, Joseph Black Building, West Mains Road, Edinburgh, Scotland EH9 3JJ, U.K.

[‡]Department of Chemistry, Graduate School of Science, and Research Center of Materials Science, Nagoya University, Chikusa-ku, Nagoya 464-8602, Japan

Supporting Information

ABSTRACT: Square planar complexes of the type $Ni(L^1)_2$, $Ni(L^2)_2$, $Cu(L^1)_2$, and $Cu(L^2)_2$, where L^1H = 2-hydroxy-5-*t*-octylacetophenone oxime and L^2H = 2-hydroxy-5-*n*-propylacetophenone oxime, have been prepared and characterized by single-crystal X-ray diffraction, cyclic voltammetry, UV/vis spectroscopy, field-effect-transistor measurements, density functional theory (DFT) and time-dependent DFT (TDDFT) calculations, and, in the case of the paramagnetic species, electron paramagnetic resonance (EPR) and magnetic susceptibility. Variation of alkyl groups on the ligand from *t*-octyl to *n*-propyl enabled electronic isolation of the complexes in the crystal structures of $M(L^1)_2$ contrasting with π-stacking interactions for $M(L^2)_2$ (M = Ni, Cu). This was evidenced by a one-dimensional antiferromagnetic chain for $Cu(L^2)_2$ but ideal paramagnetic behavior for $Cu(L^1)_2$ down to 1.8 K. Despite isostructural single crystal structures for $M(L^2)_2$, thin-film X-ray diffraction and scanning electron microscopy (SEM) revealed different morphologies depending on the metal and the deposition method (vapor or solution). The Cu complexes displayed limited electronic interaction between the central metal and the delocalized ligands, with more mixing in the case of Ni(II), as shown by electrochemistry and UV/vis spectroscopy. The complexes $M(L^2)_2$ showed poor charge transport in a field-effect transistor (FET) device despite the ability to form π-stacking structures, and this provides design insights for metal complexes to be used in conductive thin-film devices.

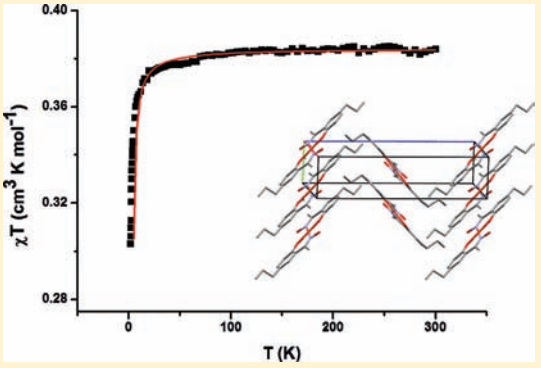

1. INTRODUCTION

Because of their diverse redox, spectroscopic, and magnetic properties, transition metal complexes are of widespread importance in the study of functional molecular materials,[1−3] with key properties including accessible oxidations/reductions,[4,5] and tunable intermolecular interactions through modification of the ligand[6] or by exchange of the transition metal ion.[7] The presence of unpaired electrons in some cases has played a key role in the extensive field of molecular magnetism and, when coupled with charge transport properties, can lead to novel magneto-conductive effects.[8−10] Metal complexes with a planar, electronically delocalized structure have proven particularly attractive for development of cooperative electronic properties because of the strong molecule−molecule interactions that can arise from π-stacking of the planar units.[11−13] This motif has led to materials showing ferromagnetism,[14] one-dimensional magnetic chains,[15] semiconductive behavior,[16,17] and a variety of structural or magnetic phase-transitions.[18] The majority of research in this field, however, has focused on well-established families of planar metal complexes such as metal-bis-1,2-dithiolenes,[19−21] metal phthalocyanines,[22] and structurally related analogues such as bis(*o*-diiminobenzosemiquinonate) nickel(II),[5,23] with much less attention given to the development of a wider variety of examples.

In this context it is important to investigate new classes of planar, electronically delocalized metal complexes or to re-evaluate appropriate existing materials previously used for a different purpose. This requires an extensive study of different classes of planar metal complexes to assess their electronic structure; their processability into thin films by evaporation or solution methods; their molecular packing in the solid state; the resulting intermolecular interactions, their magnetic properties, and the possibility of charge-transport properties. Phenolic oxime ligands are used extensively in extractive hydrometallurgy,[24−26] but the cooperative electronic properties in materials formed by transition metal complexes of these ligands has to date been overlooked. We have prepared homoleptic nickel(II) and copper(II) complexes using two structurally related phenolic oxime ligands, 2-hydroxy-5-*t*-octylacetophenone oxime (L^1H) and 2-hydroxy-5-*n*-propylacetophenone

Received: September 21, 2011
Published: November 18, 2011

   dx.doi.org/10.1021/ic2020644 | *Inorg. Chem.* 2011, 50, 12867−12876

oxime (L^2H). The size of the alkyl group at the 5-position on the aromatic ring has been varied, which affects both the solubility of the resulting complexes formed and thus the processing methods available, and also intermolecular interactions in the solid state, which determine the packing adopted by the molecules and the corresponding cooperative electronic properties that arise. We report a systematic study of the electronic, magnetic, structural, and thin-film properties of these materials to provide a thorough assessment of their potential for use in functional molecular materials and devices.

2. EXPERIMENTAL SECTION

2.1. Synthesis of Materials. All chemicals were purchased from Sigma Aldrich and used as bought without further purification.

2-Hydroxy-5-t-octylacetophenone Oxime (L^1H). Acetyl chloride (86.3 g, 1.1 mol) was added dropwise to a solution of 4-*tert*-octylphenol (206.3 g, 1 mol) in toluene (600 mL), and the resulting solution refluxed for 4 h and then stirred overnight. Aluminum trichloride (133.3 g, 1.0 mol) was added in portions to the stirred solution over 4 h, and the reaction mixture was then heated to reflux for 3 h and stirred overnight at room temperature (RT). The reaction was quenched with excess HCl (20%, 500 mL) which was added dropwise over 1 h. The organic phase was separated from the aqueous, washed with distilled water (2 × 250 mL), and filtered using phase separation paper. The solvent was removed in vacuo yielding a viscous yellow oil (230.2 g) 67% pure by GC. Hydroxylamine sulfate (221.5 g, 1.35 mol) and sodium acetate (221.4 g, 2.7 mol) were added to a solution of crude phenolic ketone (230.2 g, 0.9 mol) in ethanol (600 mL). The resulting suspension was refluxed for 2 h, allowed to cool, and poured onto toluene (500 mL) and distilled water (300 mL). The organic layer was separated, washed with distilled water (2 × 100 mL) and brine (100 mL), and filtered through phase separation paper. The solvent was removed in vacuo, and the resulting yellow solid was purified via complexation with copper, using the same general procedure as detailed below. The complex solution was stripped using sulphuric acid solution (0.1 M, 3 × 200 mL), washed with distilled water (200 mL), and filtered through phase separation paper. The solvent was removed in vacuo, and the resulting off-yellow solid was recrystallized from hexane yielding an off-white solid (135.2 g, 0.51 mol, 51% yield). ^{1}H NMR ($CDCl_3$): δ (ppm) = 0.78 (s, 9H), 1.43 (s, 6H), 1.78 (s, 2H), 2.44 (s, 3H), 7.32 (d), 7.43 (s), 7.46 (d). MS (ESI): m/z (%) = 264.20 (100%) [M^+]

2-Hydroxy-5-n-propylacetophenone Oxime (L^2H). Acetyl chloride (11.77 g, 0.15 mol) was added dropwise to a stirred solution of 4-*n*-propylphenol (13.62 g, 0.1 mol) in toluene (250 mL), and the resulting mixture was refluxed for 4 h and stirred overnight at RT. Aluminum trichloride (16.00 g, 0.12 mol) was added in 1 g portions to the stirred solution over 4 h at 10 min intervals, and the reaction was then refluxed for 3 h before being quenched with aqueous hydrochloric acid (18%, 100 mL) added dropwise over an hour. The organic layer was separated from the aqueous, washed with distilled water (2 × 50 mL), and then dried using excess magnesium sulfate. Evaporation of the solvent under reduced pressure gave an orange oil which was dissolved in ethanol (200 mL). A filtered solution of hydroxylamine hydrochloride (10.42 g, 0.15 mol) and potassium hydroxide (8.42 g, 0.15 mol) was added, and the resulting reaction mixture heated at reflux for 3 h, allowed to cool, and then poured into a toluene/water (100 mL:100 mL) solution. The organic layer was washed (50 mL water, 50 mL brine) and dried in vacuo to yield an orange oil. The salicylketoxime ligand was then recrystallized as an off-white solid (12.52 g, 65%) by cooling a concentrated *n*-heptane (50 mL) solution. ^{1}H NMR ($CDCl_3$): δ = 0.96 (t, 3H), 1.64 (m, 2H), 2.58 (t, 2H), 2.61 (s, 3H), 7.26 (d, 1H), 7.32 (s, 1H), 7.42 (d, 1H). MS (ESI): m/z (%) = 194.31 (100%) [M^+]

The same general procedure was adopted for the synthesis of all of the metal complexes. The ligand (0.02 mol) was added to a stirred solution of $Cu(OAc)_2{\cdot}H_2O$ or $Ni(OAc)_2{\cdot}4H_2O$ (0.01 mol) in ethanol (50 mL). The resulting solution was stirred for 24 h at RT, and the precipitate was collected by filtration, washed with ethanol (10 mL), then *n*-hexane (10 mL) and dried in a vacuum desiccator overnight.

Cu(L^1)$_2$. MS (ESI): m/z (%) = 588.15 (76.41%) [M^+]. Calculated for $C_{32}H_{48}CuN_2O_4$, C 65.33, H 8.22, N 4.76; found C 65.34, H 8.24, N 4.76.

Cu(L^2)$_2$. MS (ESI): m/z (%) = 447.4 (100%) [M^+]. Calculated for $C_{32}H_{28}CuN_2O_4$, C 58.98, H 6.30, N 6.25; found C 59.04, H 6.16, N 6.13.

Ni(L^1)$_2$. ^{1}H NMR ($CDCl_3$): 0.64 (s, 9H), 1.25 (s, 6H), 1.49 (s, 2H), 2.42 (s, 3H), 6.62 (d, 1H), 7.07 (d, 1H), 7.19 (s, 1H), 10.90 (s, 1H). MS (ESI): m/z (%) = 583.11 (89.08%) [M^+]. Calculated for $C_{32}H_{48}NiN_2O_4$, C 65.88, H 8.29, N 4.80; found C 65.78, H 8.95, N 4.95.

Ni(L^2)$_2$. ^{1}H NMR ($CDCl_3$): 0.96 (t, 3H), 1.64 (m, 2H), 2.40 (s, 3H), 2.57 (t, 2H), 6.94 (d, 1H), 7.12 (d, 1H), 7.24 (s, 1H). MS (EI): m/z (%) = 442.1 (100%) [M^+]. Calculated for $C_{32}H_{28}NiN_2O_4$, C 59.62, H 6.37, N 6.32; found C 59.72, H 6.30, N 6.21.

2.2. Experimental Measurements. Crystallographic data were routinely collected at 100 K. Single crystals suitable for X-ray diffraction (XRD) were prepared by various methods: $Cu(L^1)_2$ by slow evaporation of a MeOH/DCM/THF solution; $Cu(L^1)_2{\cdot}$DMSO by recrystallization from a concentrated dimethylsulfoxide (DMSO) solution; $Cu(L^2)_2$ by vapor diffusion of EtOH into a $CHCl_3$ solution; $Ni(L^1)_2$ by slow evaporation of a $(CH_3O)_2CO$ solution and $Ni(L^2)_2$ by vapor diffusion of MeCN into a $CHCl_3$ solution. A table of crystallographic data is included in the Supporting Information. Thin film XRD was carried out on a Rigaku ultraX-18HB at RT. Data were collected from 2θ angle of 5−40° at a rate of 2° per minute. Powder XRD was carried out using a Bruker AXS D8 diffractometer. Thin films were grown in a vacuum chamber on various substrates: Si (1,0,0), quartz, indium tin oxide (ITO), glass, field-effect transistor (FET) (bottom contact configuration) substrates and polyethylene terephthalate (PET). Different substrates were required for the different types of characterization: Si was used for thin film XRD and infrared spectroscopy (IR); quartz for UV/vis and scanning electron microscopy (SEM); glass for UV/vis and PET for electron paramagnetic resonance (EPR). All the substrates, except PET and the FETs, were cleaned in individual solutions of IPA, acetone, and then chloroform prior to use. Deposition was carried out via vacuum sublimation in a temperature range between 135 and 210 °C at a pressure of 2.8×10^{-4} Pa. This resulted in a growth rate of 0.1−0.3 Å/s which was monitored using a quartz crystal microbalance (QCM). The material to be sublimed was heated inside an inert crucible by applying a current. Films of approximately 100 nm thickness were produced according to the QCM. All cyclic voltammetry measurements were carried out in dry DCM using 0.3 M $TBABF_4$ electrolyte in a three electrode system, with each solution being purged with N_2 prior to measurement. The working electrode was a 0.2 mm^2 Pt wire sealed in glass. The reference electrode was Ag/AgCl calibrated against Ferrocene/Ferrocenium in the background electrolyte, and the counter electrode was a Pt rod. All measurements were made at RT using an μAUTOLAB Type III potentiostat, driven by the electrochemical software GPES. Cyclic voltammetry (CV) measurements used scan rates of 0.1 V/s, and DPV was carried out at a step potential of 0.01005 V, modulation amplitude of 0.10005 V, modulation time of 0.05 s and an interval time of 0.5 s. Solution UV/vis spectra were recorded in solution in DCM using a quartz cell of path length 1 cm on a Perkin-Elmer Lambda 9 spectrophotometer, controlled by a datalink PC, running UV/Winlab software and in thin films on a Jasco V-570 UV/vis/NIR spectrophotometer. Magnetic susceptibility measurements were performed on powder samples from 1.8 to 300 K using a Quantum Design MPMS-XL SQUID magnetometer with MPMS MultiVu Application software to process the data. The magnetic field used was 0.1 T. Diamagnetic corrections were applied to the observed paramagnetic susceptibilities by using Pascal's constants. EPR spectra were measured on a Bruker ER200D X-band spectrometer with simulations using the Bruker EPR simulation package SimFonia.[27] EPR spectra of dry DCM solutions were recorded at RT. Thin film EPR spectra were obtained on a JEOL JES-FA200 ESR Spectrometer using 100 nm films on a PET substrate

with a center field of 312 mT and a sweep width ±100 mT. Geometry optimizations of the isolated complexes, $Cu(L^2)_2$ and $Ni(L^2)_2$, were carried out at the B3LYP/6-31G(d,p) level of theory,[28−30] using Gaussian 03.[31] The X-ray crystallographic coordinates were used as the starting structures, and minima on the potential energy surface were confirmed by the absence of any imaginary frequencies. The molecular orbital isosurfaces were visualized using ArgusLab 4.0.[32] FET measurements were carried out using bottom contact devices consisting of interdigitated platinum source and drain electrodes with a silicon dioxide dielectric layer. The source and drain electrodes were 8 μm thick with a gap between the interdigitated electrodes of 2 μm. The dielectric layer was 300 nm thick, and the gate electrode was made from an n-doped silicon wafer. FET testing was done in darkness under vacuum. Imaging of thin films was carried out using a Hitachi S-4300 Scanning Electron Microscope.

3. RESULTS AND DISCUSSION

The salicylketoxime ligands discussed in this work are planar, bidentate, and bind through two heteroatoms making them interesting candidates for investigation to assess their potential in magnetic or conducting materials. Synthesis of both Ni and Cu complexes of two different phenolic oxime ligands was readily achieved by direct reaction of the metal acetate salt with the protonated ligand in ethanol (Figure 1), enabling

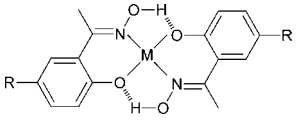

Figure 1. Molecular structure of the four complexes, M = Ni, Cu; R = *t*-octyl (L^1), *n*-propyl (L^2).

comparison of the role of the central metal in the electronic properties, and the role of the alkyl chain in the packing properties of the molecules. The complexes achieve good stability through the pseudomacrocylic arrangement arising from hydrogen bonding between the oximic hydrogen and the phenolic oxygen of the opposing ligands.

3.1. Crystal Structures. In the crystal structures of the four unsolvated complexes, $Cu(L^1)_2$, $Ni(L^1)_2$, $Cu(L^2)_2$, and $Ni(L^2)_2$, the metal atom lies on a crystallographic inversion center which results in perfectly planar $N_2O_2^{2-}$ donor sets. Bond lengths and angles and the chelate bite distances in the coordination sphere, together with the O···O contact distances in the outer sphere which are associated with oxime OH to phenolate oxygen hydrogen bond, are shown below (Table 1). As noted previously,[24] the bond lengths to the Ni(II) atom are significantly shorter than those to the Cu(II) atom. As might be expected,[33] the $N_2O_2^{2-}$ donor set forms longer bonds to the Cu(II) atom in the DMSO adduct, $[Cu(L^1)_2DMSO]$ (Figure 2), which has a five coordinate square pyramidal structure. The

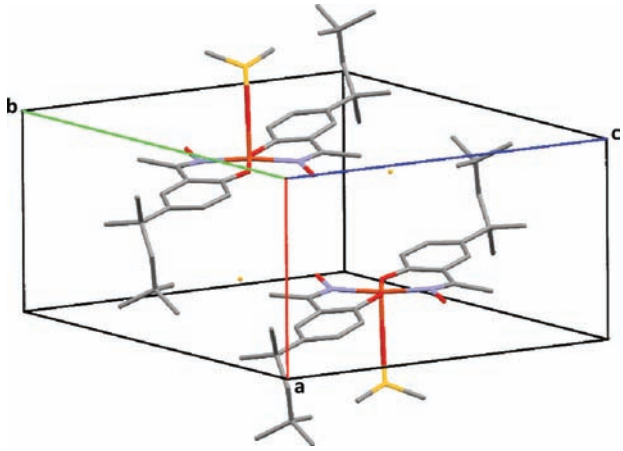

Figure 2. Unit cell of $Cu(L^1)_2$.DMSO. Hydrogen atoms have been omitted for clarity and only the higher occupancy site of the disordered $(CH_3)_2S$ unit of the DMSO is shown.

bite angle is larger in the Ni(II) complexes, which is a consequence of the shorter Ni−O and Ni−N bonds requiring the metal atom to move toward the center of the N···O bite.

The crystal packing of $Cu(L^1)_2$ and $Ni(L^1)_2$ are compared in Figure 3. Because of the bulky *t*-octyl chains, π-overlap of the

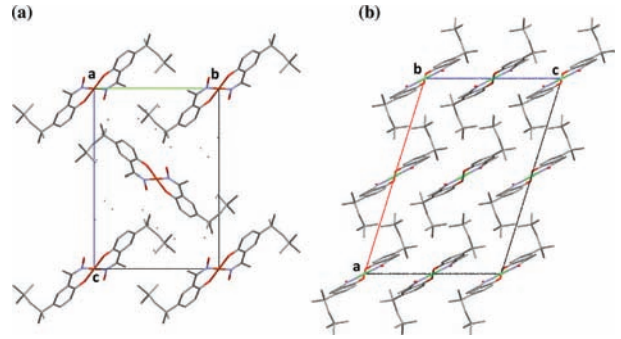

Figure 3. Unit cells of (a) $Cu(L^1)_2$ viewed along the *a*-axis and (b) $Ni(L^1)_2$ viewed along the *b*-axis. Hydrogen atoms have been omitted for clarity, and only the higher occupancy site of one of the octyl groups, which is disordered in $Cu(L^1)_2$, is shown.

Table 1. Selected Bond Length and Angles

	$[Cu(L^1)_2 \cdot DMSO]^a$					
	part *a*	part *b*	$Cu(L^1)_2$	$Ni(L^1)_2$	$Cu(L^2)_2$	$Ni(L^2)_2$
M−O (Á)	1.919(2)	1.901(3)	1.870(1)	1.819(1)	1.883(1)	1.827(1)
M−N (Á)	1.957(4)	1.964(4)	1.962(1)	1.883(2)	1.948(2)	1.883(1)
O−M−N (deg)	89.7(1)	90.5(1)	91.05(5)	92.12(6)	91.84(7)	92.40(5)
O−M−N′ (deg)	89.5(1)	88.9(1)	89.95(5)	87.88(6)	88.16(7)	87.60(5)
N···O bite distance (Á)	2.745(5)	2.733(5)	2.735(2)	2.666(2)	2.753(2)	2.678(2)
MO···OH	2.598(4)	2.591(4)	2.583(2)	2.482(2)	2.551(2)	2.471(1)

[a]This complex has no crystallographically imposed symmetry and two lengths and angles associated with the chelate units ***a*** and ***b*** in Supporting Information, Figure S3 are shown. The DMSO oxygen atom forms a bond to Cu of 2.229(3) Á and defines angles of 93.8(1), 98.3(1), 95.2(1), and 91.9(1)° with atoms O_2, O_{45}, N_6, and N_{81}.

dx.doi.org/10.1021/ic2020644 | *Inorg. Chem.* 2011, 50, 12867−12876

planar portions of the molecules is not favored and the interplanar distance between overlapping aromatic rings is 6.97 Å in $Cu(L^1)_2$·DMSO, 7.58 Å in $Cu(L^1)_2$, and 7.12 Å in $Ni(L^1)_2$.

$Ni(L^2)_2$ and $Cu(L^2)_2$ are isomorphous and, in contrast to $M(L^1)_2$, display a herringbone packing motif with the π-stacking of the molecules extending along the *b*-axis in a regular stack (Figure 4). The interplanar packing distance is slightly longer, 3.22 Å, in $Ni(L^2)_2$ than in $Cu(L^2)_2$, 3.17 Å.

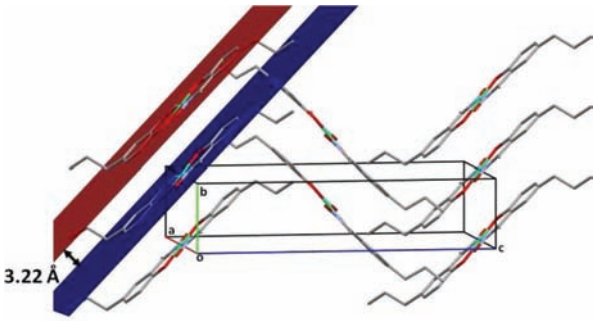

Figure 4. Crystal packing of $Ni(L^2)_2$. The mean planes (red and blue) have been calculated using both aromatic rings on each molecule using the program Mercury 2.3.[34−37] Hydrogen atoms have been omitted for clarity.

The steric effects of the ^{t}octyl or ^{n}propyl substituents clearly have an impact on the solid state packing of the complexes. The complexes of L^2 form a stack with short intermolecular distances suggesting strong π-stacking interactions, whereas those formed from L^1H have larger interplanar distances, too great for effective π-overlap. This presents an opportunity to investigate the effect of intermolecular π-stacking interactions on magnetic and conduction properties, as the L^1H/L^2H pairs share a common core electronic structure. It provides a comparison between materials composed of essentially electronically identical molecules that interact in the solid state with those that are effectively isolated.

3.2. Electrochemistry. Both the ligands were studied in the range of −2 to 2 V at various scan rates and both display similar behavior. The cyclic voltammetry (CV) measurements (Table 2) indicate that L^1H and L^2H are oxidized irreversibly at

Table 2. Electrochemical Data Measured by CV and DPV[a]

	cyclic voltammetry		differential pulse voltammetry	
sample	E_{pc} (V)		E_{pc} (V)	
L^1H	1.40	1.80	1.32	1.75
L^2H	1.42	1.78	1.34	1.71
$Cu(L^1)_2$	1.43	1.80	1.22	1.72
$Ni(L^1)_2$	1.29	1.82	1.24	1.74
$Cu(L^2)_2$	1.40		1.27	1.82
$Ni(L^2)_2$	1.35		1.20	1.73

[a]Supporting Information, Figures S5−S10. The second oxidation process was not well-defined in complexes $Cu(L^2)_2$ and $Ni(L^2)_2$ by CV.

1.41 and 1.42 V. L^2H displays another irreversible oxidation at 1.78 V which is not as well-defined in the CV voltammogram of L^1H.

The voltammograms of the complexes (Figure 5) are very similar to those of the uncomplexed ligands, which implies that the redox processes involved are predominantly ligand based.

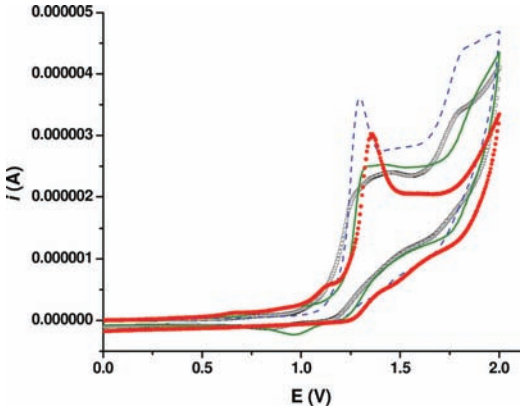

Figure 5. Cyclic voltammetry of complexes $Cu(L^1)_2$ [open squares], $Ni(L^1)_2$ [blue dashed lines], $Cu(L^2)_2$ [green lines] and $Ni(L^2)_2$ [red solid circles], at a scan rate of 0.1 V/s between 0 and 2 V.

Each complex exhibits an irreversible oxidation occurring at approximately the same potential, indicating that the highest occupied molecular orbital (HOMO) of each complex is substantially localized on the ligand. Replacement of the phenolic protons by Ni^{2+} has little effect on the redox processes compared with the free ligands ,and no other redox processes have been generated through the redox activity of the metal. None of the samples displayed a reduction process between 0 and −2 V.

3.3. UV/vis Spectroscopy. The UV−vis spectra of the ligands, L^1H and L^2H, in the range 250−800 nm (Supporting Information, Figure S11) are very similar. Both spectra are dominated by a strong absorption band occurring at 315 nm, assigned as a $\pi-\pi^*$ transition. The bis-ligand Ni(II) and Cu(II) complexes formed from L^1H and L^2H have also been studied by UV−vis absorption spectroscopy (Figure 6). The absorption

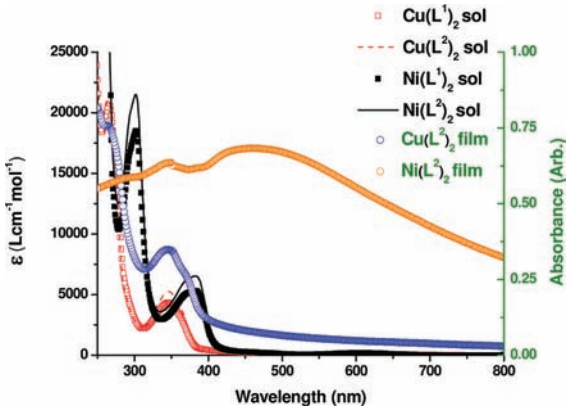

Figure 6. UV/vis spectra of DCM solutions of the complexes overlaid with thin film absorption spectra of $M(L^2)_2$ complexes on SiO_2 substrates (arbitrary absorbance units).

spectra for the Ni and Cu complexes are similar in overall structure; however, there is a marked red shift in the Ni spectra relative to that of Cu. The spectra for both Ni complexes are almost identical, and are dominated by a strong absorption band at 305 nm, with a weaker band observed at 383 nm whereas the Cu spectra for both complexes show a prominent UV band around 260 nm, with a weaker band appearing around 346 nm. At high concentrations all of the complexes display Laporte forbidden d-d transitions in the region 606−654 nm.

dx.doi.org/10.1021/ic2020644 | *Inorg. Chem.* 2011, 50, 12867−12876

The more intense bands centered between 346 and 383 nm (Figure 6) are assumed to be predominantly intraligand in character, but their energies are dependent on the nature of the complexed metal. The difference in energy of the UV absorptions when comparing the Cu and Ni complexes indicates a metal orbital contribution to the transition, while the differing alkyl groups exert only a minimal influence. These transitions are in the same general range as that witnessed in the free ligand, indicating metal and ligand orbital mixing is limited, although noticeably greater for Ni than for Cu.

The electronic absorption spectra of 100 nm thin films of the $M(L^2)_2$ complexes on quartz are shown in Figure 6. The thin film spectrum of the Cu(II) complex closely resembles its solution spectrum but for the Ni(II) complex there is a noticeable degree of red shifting. The lack of red shifting in the Cu(II) could infer that the intermolecular interactions in the solid state are weaker, attributed to the different metal ions affecting intermolecular interactions. For example, with the Ni(II) complexes, the larger involvement of the metal in the frontier orbitals of the individual molecules may facilitate stronger orbital interaction between molecules.

3.4. Computational Procedures. To estimate the energies of the HOMO and the lowest unoccupied molecular orbital (LUMO) in our complexes, single molecule gas phase calculations were carried out at the B3LYP/6-31G(d,p) level of theory for complexes $Cu(L^2)_2$ and $Ni(L^2)_2$. The extended alkyl chain on the L^1H complexes is not expected to alter the electronic properties significantly from that of the L^2H complexes. The results (inset Figure 7) indicate that the

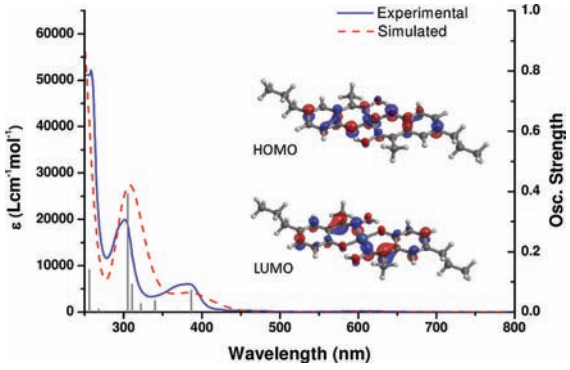

Figure 7. Time dependent DFT generated UV−vis spectrum (red dashed lines) overlaid with the experimental spectrum (blue solid lines) of $Ni(L^2)$.

HOMO of $Ni(L^2)_2$ is of mixed metal/ligand character and is delocalized over both the aromatic part of the molecule and the Ni(II) center. They also show that the LUMO is localized solely on the ligand. The energy of the HOMO has been calculated as −5.18 eV and the LUMO is −1.33 eV. The energies of the frontier orbitals and the large HOMO−LUMO gap of 3.85 eV is consistent with the observation of accessible oxidation but no accessible reduction in the electrochemistry.

The electronic transitions witnessed in solution have been assigned using time dependent DFT, with the simulated spectra in good agreement with that obtained experimentally (Figure 7). The transition at 383 nm has been assigned as being from the HOMO to LUMO (92%) whereas the transition at 305 nm is from HOMO-2 to LUMO (62%) and HOMO-3 to LUMO (24%). The HOMO is composed of Ni(d_{yz}) and Lπ character with the LUMO assigned as a Lπ* orbital. The HOMO-2 is of mixed metal(d_{xz}) and ligand character, but the HOMO-3 is solely based on the d_{z^2} orbital.

3.5. SOMO Wrestling. The calculation of the electronic structure of copper containing complexes continues to be a challenge for electronic structure methods. Recent work on Cu-phthalocyanines has shown that the predicted electronic structure, particularly the ordering of the occupied valence orbitals, is sensitive to the level of theory applied, and in the case of DFT, sensitive to the nature of the functional employed.[38−41] While in most cases the unpaired electron is calculated to reside in the Cu-based $d_{x^2-y^2}$ orbital, in agreement with experimental evidence from EPR measurements,[42,43] contradictory predictions place it variously above and below the doubly occupied HOMO orbital.

In the course of this work, similar effects were also observed for the copper complexes, where not just the electronic structure, but the geometrical structure was seen to be sensitive to the nature of the functional chosen. Relatively large basis sets 6-31+g(d,p) and cc-pVTZ were used in combination with a number of functionals to investigate the sensitivity of the electronic structure to the level of theory (Supporting Information, Table S3). Of the functionals under study, the "pure" functionals (OLYP, OPBE, PBE, SVWN, and BLYP) tend to place the SOMO within the HOMO−LUMO gap, predicting that the lower energy HOMO is a doubly occupied ligand-based π-orbital. HF and the hybrid and long-range corrected functionals (B3LYP, M06-HF, PBE1PBE, BH and HLYP, CAM-B3LYP), in contrast, tend to place the SOMO at an energy below the doubly occupied ligand-based π HOMO. In the case of OLYP, OPBE, PBE and B3LYP(VWN5) the geometry of the copper complexes was predicted to be significantly nonplanar around the Cu center.

Recent work by Kronick et al.[44] has suggested the self-interaction error, inherent in the majority of DFT functionals, is responsible for the difference in the electronic structures predicted by local and hybrid functionals. The self-interaction error, which is more pronounced in the nonhybrid functionals, tends to destabilize more localized orbitals, in this case the singly occupied Cu-based $d_{x^2-y^2}$ orbital, raising it in energy above the doubly occupied ligand-based HOMO. When a fraction of HF exchange is included in the hybrid functionals the self-interaction error is reduced, and the Cu-based $d_{x^2-y^2}$ orbital is calculated to lie lower in energy than the HOMO (Supporting Information, Figure S12, Table S3).

Irrespective of the functional employed, all computational methods consistently predict that the unpaired electron does indeed reside in the mainly Cu-based $d_{x^2-y^2}$ orbital, consistent with the experimental EPR results (vide infra). The insensitivity of the electrochemical redox peaks to the choice of central metal atom and the lack of an observable oxidation from the Cu(II) SOMO also supports a doubly occupied ligand based orbital as the HOMO. Figure 10 (inset) depicts the calculated spin density of the unpaired electron on the Cu(II) complex using the B3LYP/6-31G(d,p) level of theory. As expected the unpaired electron appears to be based in the $d_{x^2-y^2}$ orbital of the metal, with some delocalization onto the donor atoms of the ligand.

3.6. Thin Film XRD. Complexes of the type $M(L^2)_2$ were found to be volatile, and thin films on various substrates have therefore been prepared by sublimation under reduced pressure. XRD measurements were carried out at RT between angles of 5° and 40° (2θ). Infrared (IR) spectroscopy carried out on these films indicates that the thin films are structurally

dx.doi.org/10.1021/ic2020644 | Inorg. Chem. 2011, 50, 12867−12876

the same as the powder sample prior to deposition (Supporting Information, Figure S1, S2). This also reassures us that sample decomposition has not taken place during volatilization.

XRD measurements carried out on powder samples of $Cu(L^2)_2$ matches the calculated powder pattern generated from the single crystal data indicating the bulk powder is in the same crystallographic phase as that which was isolated from solution as a single crystal. However, XRD measurements on powdered $Ni(L^2)_2$ appears to show additional peaks that do not correspond to the structure obtained from the single crystal data. This indicates that the sample contains a mixture of crystallographic phases or a trace amount of a crystalline impurity.

Shown in Figure 8 is the thin film XRD of $Cu(L^2)_2$ on a Si wafer. Contrasting it with the predicted powder pattern appears

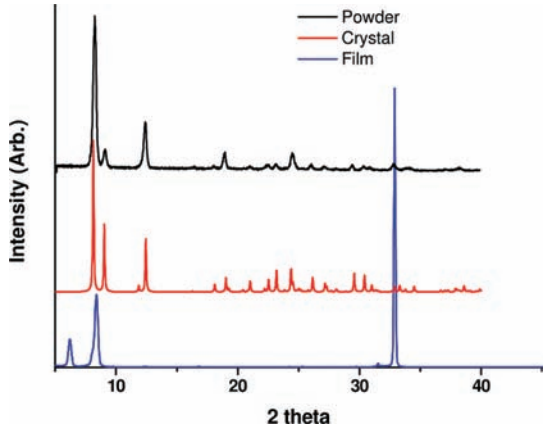

Figure 8. Out of plane thin film XRD of $Cu(L^2)_2$ on a Si substrate (blue) overlaid with the calculated powder pattern from the single crystal data (red) and the experimental powder pattern (black).

to suggest a different crystallographic phase in the thin film from that present in the single crystal. Note that the intense peak at 33° (2θ) is due to the substrate. The large peaks at 6.18° and 8.38° (2θ) in the thin film XRD correspond to a *d*-spacing of 14.28 and 10.54 Å, respectively, but have not been indexed because of the lack of distinct peaks available. From the single crystal data, the intense peaks at 8.13, 9.00, and 12.45° correspond to a *d*-spacing of 10.86, 9.81, and 7.10 Å, respectively. These peaks are due to reflection from the (100), (002), and (102) planes.

As witnessed with the Cu(II) complex, the analogous Ni(II) sample also appears to exhibit a different structure when thermally grown on a Si thin film, as can be observed in Figure 9. The prominent peaks at 8.04 and 10.47° (2θ) correspond to an intermolecular *d*-spacing of 10.98 and 8.23 Å, respectively. Contrasting this with the single crystal data, the dominant peaks are at 8.13, 8.92, and 12.30°, similar to the thin film obtained from the volatile Cu(II) complex, with the same assignment of planes.

From the single crystal XRD data the $Cu(L^2)_2$ and $Ni(L^2)_2$ complexes appear isomorphous but on a thin film these materials are clearly exhibiting a different phase to each other. The single crystal data have all come from solution grown samples but to explore the possibility of polymorphism from vapor grown samples, attempts to isolate single crystals by sublimation methods have been made. However, crystals grown thus far have not been of a suitable quality for single crystal analysis.

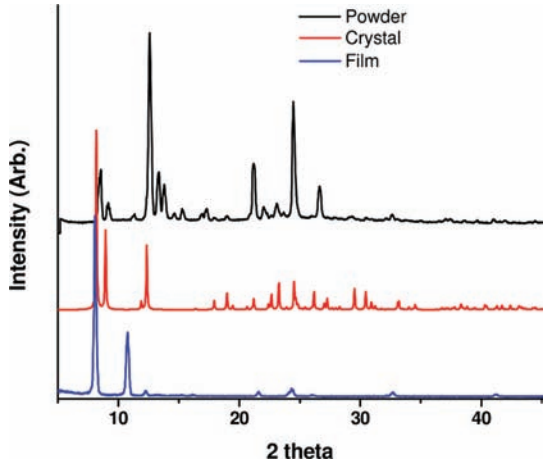

Figure 9. Out of plane thin film XRD of $Ni(L^2)_2$ on a Si substrate (blue) overlaid with the calculated powder pattern from the single crystal data (red) and the experimental powder pattern (black).

3.7. Magnetic Susceptibility. Measurements carried out on a powder sample of $Cu(L^1)_2$ are shown in Supporting Information, Figures S16 and S17, which clearly indicates paramagnetic behavior exhibited by the sample with no indication of any significant magnetic ordering or interactions at low temperature. This result is expected because of the steric bulk of the tertiary octyl chain present on the ligand, L^1H. The steric effect of the ligand on the crystal packing results in a large intermolecular distance between Cu(II) centers, approximately 7 Å, such that the molecule behaves as an isolated paramagnet.

Fitting to the Curie–Weiss law in the range 1.8–300 K (Supporting Information, Figure S16) the Curie constant has been determined as 0.3794 cm^3 K mol^{-1}, leading to a g factor of 2.012, and the Weiss constant as 0.0118 K. Because of the spin orbit coupling present in Cu(II), the g-value is often anisotropic and typically lies between 2.0 and 2.30.[45] As the g factor is close to the free electron value of 2.002, this would suggest the unpaired electron has significant ligand character.

At low temperature the χT vs T plot for $Cu(L^2)_2$ shows a downward trend indicating the metal centers are interacting antiferromagnetically (Figure 10). Treating the sample as a 1-D chain of interacting $S = 1/2$ molecules, the experimental data were fit to the Bonner–Fisher expression[46] modified by Estes et al.[47] This calculates the isotropic g-value as 2.024 and J as 0.49 cm^{-1}. The small J value indicates a weak antiferromagnetic coupling, giving a susceptibility peak at about 6 K. The g-value is rather low; however this is consistent with the Curie–Weiss fit and with the behavior of $Cu(L^1)_2$.

The outcome of modifying the alkyl chain on the chelating ligand can be directly seen by comparing the magnetic data; the small ^{n}propyl chain has caused the interplanar distance to shorten to allow π–π stacking between molecules and as a result the Cu(II) centers can now interact magnetically. The change from paramagnetic behavior in $Cu(L^1)_2$ to weak antiferromagnetic coupling in $Cu(L^2)_2$ can be attributed to the interplanar distance shortening to ~3 Å in $Cu(L^2)_2$ from ~7 Å in $Cu(L^1)_2$.

3.8. EPR. Because of experimental limitations in magnetic susceptibility measurements, a more accurate estimation of the g-value is obtained from EPR. Measurements have been carried out on solution samples of both Cu(II) complexes at RT. In the case of $Cu(L^1)_2$, the EPR signal is split into a quartet of triplets owing to the Cu nuclear spin of 3/2 (quartet) and ^{14}N spin of 1

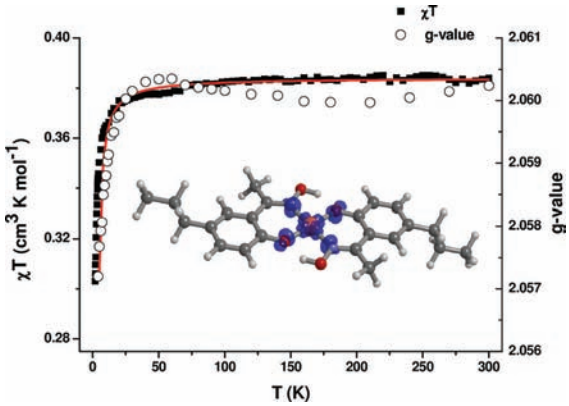

Figure 10. χT vs T plot of $Cu(L^2)_2$ from 1.8−300 K. The Bonner−Fisher model curve (red line) displays a good fit to the experimental data (black squares). The curve has been corrected for a temperature independent paramagnetic parameter of 3.15×10^{-4} cm^3 mol^{-1}. Powder EPR of $Cu(L^2)_2$ showing the change in g-factor with temperature (hollow circles) has been overlaid. Inset is the calculated spin-density at the B3LYP/6-31G(d,p) level of theory.

(triplet). Note that both isotopes of Cu have the same nuclear spin. From the EPR simulation, the following values have been determined: coupling to the ^{63}Cu nuclei of 90.5 G, coupling to the ^{65}Cu nuclei of 94.5 G, coupling to both the ^{14}N nuclei of 14.3 G, a line width of 10.0 G and g_{iso} of 2.11. At lower magnetic field the resolution of the hyperfine coupling is not well resolved and thus simulation is only possible for the resolved part of the spectrum at higher magnetic field; a higher frequency EPR experiment may improve the resolution. The coupling of the unpaired electron to the ^{14}N nucleus indicates that in the complex it is not completely localized on the Cu(II) center but some of the electron density is on the N donor atoms of the ligand, which implies that the SOMO of the complex is delocalized onto part of the ligand. This is consistent with the computational results above. The simulated g factor is slightly larger than that determined by fit to the susceptibility data although broadly consistent.

A similar spectrum was obtained for $Cu(L^2)_2$, (Figure 11), indicating as expected that the paramagnetic systems are closely related. From the EPR simulation, the following values have been determined: coupling to the ^{63}Cu nuclei of 90.5 G, coupling to the ^{65}Cu nuclei of 96.5 G, coupling to both the ^{14}N nuclei of 15.8 G, a line width of 10.0 G and g_{iso} of 2.10. Again we see a delocalization of the SOMO onto the N donor on the ligand, the extent of which is almost identical to $Cu(L^1)_2$ by estimation from the simulation parameters. Complexes such as Cu(II) tetraphenyl porphyrin (TTP) have been previously studied by EPR[42] and reported to have an average metal coupling of 95 G, ^{14}N coupling of 14 G and a g-factor of 2.117. In this Cu(TTP) example where the spin is based in the $d_{x^2-y^2}$ orbital, the simulation parameters closely match that of our system implying the unpaired electrons are in similar environments with similar delocalization onto ligand orbitals.

The powder EPR results of $Cu(L^2)_2$, (Figure 10), display how the g-factor changes as the material magnetically orders at low temperature. In this case the g-factor indicates a greater degree of electron delocalization than was estimated by simulation from the solution measurement. The value falls from approximately 2.060 to almost 2.057 as the antiferromagnetic interactions become more significant at lower temperature. Reassuringly, the change in g-factor broadly

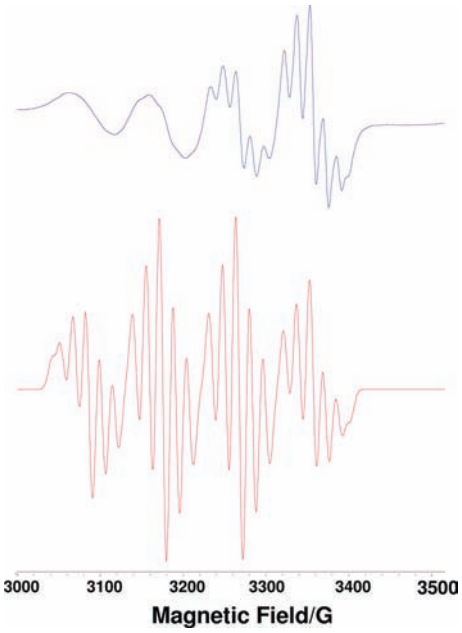

Figure 11. Solution EPR results for $Cu(L^2)_2$ (upper) and simulated spectrum (lower). Measurement carried out in DCM at 25 °C.

resembles the χT vs T data from magnetic susceptibility measurements. This reaffirms that using a sterically smaller ligand is having the desired effect on the intermolecular interactions in the solid state.

3.9. SEM Imaging. The performance of a thin film device, such as a transistor, can be influenced by crystallinity and grain boundaries[48,49] so SEM has been carried out to investigate the thin film morphology. The Ni(II) and Cu(II) complexes appear to exhibit different morphologies to each other on both ITO and Si. The Cu(II) crystals appear needle like in shape while the Ni(II) film consists of crystallites of various shapes with less even coverage of the substrate. SEM images of the thin films on Si, ITO, and FET substrates at different magnifications (Figure 12, Supporting Information, Figure S19), highlight that the Ni(II) complex has not formed homogeneous films. The source-drain gap of our FET substrates (vide infra) is only 2 μm so the films, although not ideal, should still be suitable for FET studies. Both films were formed under similar conditions, but a higher temperature was reached in the deposition of $Cu(L^1)_2$ and this may be responsible for the pronounced change in morphology. Both films were deposited at a rate of 0.1−0.3 Å per second but in the deposition of $Cu(L^2)_2$ a maximum temperature of 213 °C was reached as opposed to 157 °C in the deposition of $Ni(L^2)_2$.

The solution deposited materials, in contrast to the vacuum grown films, form large needle-like crystallites much bigger than those which are formed by sublimation. The solution grown crystallites effectively bridge the source-drain gap of 2 μm whereas not all the vacuum deposited particles are this large.

3.10. FET Measurements. A series of FET measurements was carried out using the less sterically hindered, $M(L^2)_2$, complexes to form thin films by both vapor processing and solution coating. From the cyclic voltammetry it appears that these materials are weak electron donors therefore p-type conduction may be expected. However, none of these complexes produced gate voltage effects when measurements were carried out using the FET configuration described earlier (see for example Supporting Information, Figure S20). Instead

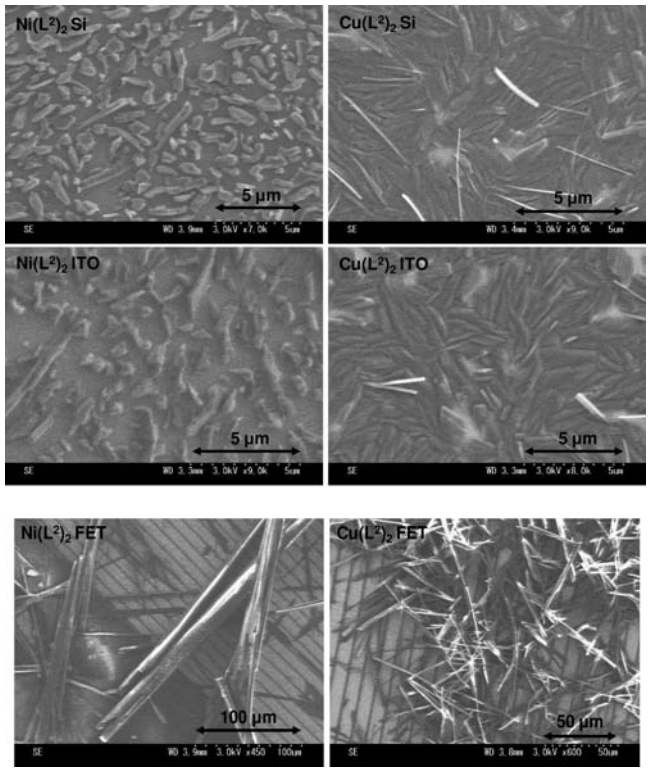

Figure 12. SEM images of the volatile complexes on Si and ITO substrates (upper four images). Also shown at the bottom are drop coated samples deposited onto FET interdigitated electrodes with a 2 μm gap. Samples were drop coated from saturated solutions of DCM. Scale shown inset.

each material exhibited insulating behavior under a gate potential in an FET device, despite the films being highly crystalline and the π-stacking capability designed into the complexes. The poor performance may be due to an unfavorable arrangement of the molecules in the solid state; however, a likely contributing factor is the lack of significant mixing of metal d-orbitals with the ligands' frontier orbitals, particularly for the Cu(II) complexes. The lack of mixing will limit the delocalization of any introduced holes over the molecule shown by the little difference between the oxidation potential of the metal complexes and the uncomplexed ligand. In addition, the localized ligand orbitals which result will limit the intermolecular interactions required for charge transport.

3.11. Discussion. Although phenolic oxime complexes have been extensively studied in metal extraction technology, systematic study of their electronic properties has been overlooked, despite their similarity to planar metal complexes under investigation in molecular magnetic and semiconducting materials. Variation of the alkyl substituent *para* to the hydroxyl group in 2-hydroxy-acetophenone oxime has allowed us to control the extent of intermolecular interactions in the Ni(II) and Cu(II) complexes. A bulky alkyl substituent electronically isolates the molecules in the solid state, while a smaller alkyl chain allows short intermolecular distances, as witnessed by comparisons of their single crystal X-ray structures, while still retaining sufficient solubility to enable solution processing. We have also shown these materials to be volatile and processable via vacuum sublimation methods, consistent with the stability imposed through the pseudomacrocyclic structure.

From the electrochemical studies, absorption spectroscopy, and the computational work, the materials appear to have a large energy gap between the HOMO and LUMO, and the electrochemical processes, within the solvent window, are irreversible. FET results indicate that these materials are poor conductors and likely not suitable for this application. In keeping with this, computational, EPR, and magnetic measurements on the Cu(II) complexes have indicated that intermolecular interactions are weak, which is affirmed by thin film absorption spectroscopy. The poor FET performance appears, in part, attributable to the minimal mixing of metal d-orbitals with the ligands frontier orbitals, and consequently the lack of facile redox processes. This lack of strong orbital overlap within the molecule, evidenced by the electrochemical data, may also play a role in the weak intermolecular interactions.

To maximize intermolecular interactions between frontier orbitals and to ensure accessible oxidation and reduction processes, significant delocalization across the molecule is desirable. In metal-phthalocyanine complexes for example, extensive delocalization is already inherent in the free-base compound, and addition of the metal center is not required to play a specific role in enhancing delocalization. This contrasts with metal-*bis*-1,2-dithiolene complexes where the metal plays a key role in mediating orbital mixing of the two dithiolene ligands across the complex to provide an extended, delocalized system. Hence, in dithiolene complexes, the identity of the central metal and resulting orbital energies is crucial in determining molecular electronic properties. The phenolic oxime ligands studied here fall into the latter category where the metal is required to play an electronic role in mediating delocalization across the complex. However, in the case of Ni(II) and especially Cu(II), the metal does not fulfill that role.

EPR spectroscopy indicated a largely Cu(II) centered radical, with a similar degree of metal−ligand spin density distribution to that of a Cu-porphyrin complex with some spin density delocalized onto the donor nitrogen atoms. In such Cu(II) complexes, we noted the computational complexity that has previously been observed regarding the relative energy of the SOMO compared with the other orbitals. Experimentally, the electrochemical observation of ligand-based oxidation rather than Cu-centered oxidation suggests a doubly occupied ligand-based HOMO as the highest orbital. Our extensive survey of different levels of theory has given guidance on the ability of different methods to generate theoretical results consistent with this interpretation. This assessment of a range of functionals will aid future computational study of other similar Cu(II) coordination complexes.

Still of interest is the characterization and further study of the thin film crystal packing, in particular how the magnetic properties alter with crystal packing. The SEM results, coupled with thin-film XRD, have shown visually how deposition technique and substrate can have a major impact on the film morphology and crystal size, but further exploration of how the deposition conditions affects thin film morphology is required to attempt to understand the thin film polymorphism.

4. CONCLUSIONS

We have prepared a series of metal phenolic oxime complexes designed to probe the role of (i) the central metal and (ii) the peripheral alkyl in determining both the intrinsic electronic properties of the molecules and the structural packing that leads to intermolecular interactions and resulting materials properties. Through extensive electronic, structural, thin-film, and

materials characterization, a thorough assessment has been possible of the potential of this class of molecules in functional devices and by implication insight has been gained into the design of such metal complexes in general. We successfully showed control of intermolecular π-stacking interactions by alteration of the peripheral alkyl chain. Despite this processing control however, intermolecular magnetic interactions remained weak and no evidence of charge transport between molecules was observed in an FET. We attribute this mainly to the limited mixing of the metal and ligand orbitals.

Design of new families of metal complexes suitable for functional materials should therefore focus on a good energetic match between orbitals of the metal and the delocalized ligand, or should select polydentate or macrocyclic ligands that already possess extensive delocalization analogous to the properties of phthalocyanines, leading to more redox activity and more delocalized frontier orbitals. Application of the structural and processing control through alkyl-chain variation, along with the electronic influence of the central metal achieved in this work, to molecules where greater metal−ligand orbital mixing is evident will lead to systems where the unique properties of metal complexes in semiconducting devices can be fully realized.

■ ASSOCIATED CONTENT

Ⓢ Supporting Information

Crystallographic data in CIF format. Further details are given in Tables S1−S3 and Figures S1−S20. This material is available free of charge via the Internet at http://pubs.acs.org.

■ AUTHOR INFORMATION

Corresponding Author

*Fax: +44 (0)131 650 4743. Phone: +44 (0)131 650 4755. E-mail: neil.robertson@ed.ac.uk.

■ ACKNOWLEDGMENTS

We thank the EPSRC and the Japanese Science and Technology agency (JST) for funding. This work has made use of the resources provided by the EaStChem Research Computing Facility (http://www.eastchem.ac.uk/rcf). This facility is partially supported by the eDIKT initiative (heep://www.edikt.org).

■ REFERENCES

(1) McKeown, N. B. *Phthalocyanine Materials: Synthesis, Structure and Function*; Cambridge University Press: Cambridge, U.K., 1998.
(2) *Dithiolene Chemistry: Synthesis, Properties, and Applications*; Stiefel, E. I., Ed.; John Wiley & Sons: Hoboken, NJ, 2004; Vol. *52*, p 1- 738.
(3) Long, N. J. *Metallocenes: An introduction to sandwich complexes*. Blackwell Science Ltd: Oxford, U.K., 1998.
(4) Wada, H.; Taguchi, T.; Noda, B.; Kambayashi, T.; Mori, T.; Ishikawa, K.; Takezoe, H. *Org. Electron.* **2007**, *8*, 759−766.
(5) Shin-ichiro, N.; Taishi, T.; Yoshihiro, I.; Ho-Chol, C.; Susumu, K.; Tomoyuki, A.; Takayoshi, N. *Adv. Mater.* **2008**, *20*, 3399−3403.
(6) Robertson, N.; Cronin, L. *Coord. Chem. Rev.* **2002**, *227*, 93−127.
(7) Bao, Z.; Lovinger, A. J.; Brown, J. *J. Am. Chem. Soc.* **1998**, *120*, 207−208.
(8) Uji, S.; Shinagawa, H.; Terashima, T.; Yakabe, T.; Terai, Y.; Tokumoto, M.; Kobayashi, A.; Tanaka, H.; Kobayashi, H. *Nature* **2001**, *410*, 908−910.
(9) Fujiwara, H.; Kobayashi, H.; Fujiwara, E.; Kobayashi, A. *J. Am. Chem. Soc.* **2002**, *124*, 6816−6817.
(10) Kobayashi, H.; Sato, A.; Arai, E.; Akutsu, H.; Kobayashi, A.; Cassoux, P. *J. Am. Chem. Soc.* **1997**, *119*, 12392−12393.
(11) Shimazaki, Y.; Yajima, T.; Takani, M.; Yamauchi, O. *Coord. Chem. Rev.* **2009**, *253*, 479−492.
(12) Jia, J.; Hubberstey, P.; Champness, N.; Schröder, M.; Hosseini, M. W. *Supramolecular Chemistry of 4,4′-Bipyridine-N,N′-dioxide in Transition Metal Complexes: A Rich Diversity of Co-ordinate, Hydrogen-Bond and Aromatic Stacking Interactions*; Springer: Berlin/Heidelberg, Germany, 2009; Vol. *132*, pp 135−161.
(13) Ye, B.-H.; Tong, M.-L.; Chen, X.-M. *Coord. Chem. Rev.* **2005**, *249*, 545−565.
(14) Coomber, A. T.; Beljonne, D.; Friend, R. H.; Bredas, J. L.; Charlton, A.; Robertson, N.; Underbill, A. E.; Kurmoo, M.; Day, P. *Nature* **1996**, *380*, 144−146.
(15) Staniland, S. S.; Fujita, W.; Umezono, Y.; Awaga, K.; Camp, P. J.; Clark, S. J.; Robertson, N. *Inorg. Chem.* **2005**, *44*, 546−551.
(16) Dalgleish, S.; Yoshikawa, H.; Matsushita, M. M.; Awaga, K.; Robertson, N. *Chem. Sci.* **2011**, *2*, 316−320.
(17) Navor, N. L.; Robertson, N.; Weyland, T.; Kilburn, J. D.; Underhill, A. E.; Webster, M.; Svenstrup, N.; Becher, J. *J. Chem. Soc., Chem. Commun.* **1996**, 1363.
(18) Pei, W.-B.; Wu, J.-S.; Tian, Z.-F.; Ren, X.-M.; Song, Y. *Inorg. Chem.* **2011**, *50*, 3970−3980.
(19) Mercuri, M. L.; Deplano, P.; Pilia, L.; Serpe, A.; Artizzu, F. *Coord. Chem. Rev.* **2010**, *254*, 1419−1433.
(20) Cho, J.-Y.; Domercq, B.; Jones, S. C.; Yu, J.; Zhang, X.; An, Z.; Bishop, M.; Barlow, S.; Marder, S. R.; Kippelen, B. *J. Mater. Chem.* **2007**, *17*, 2642−2647.
(21) Deplano, P.; Pilia, L.; Espa, D.; Mercuri, M. L.; Serpe, A. *Coord. Chem. Rev.* **2010**, *254*, 1434−1447.
(22) Bao, Z.; Lovinger, A. J.; Dodabalapur, A. *Appl. Phys. Lett.* **1996**, *69*, 3066−3068.
(23) Noro, S.-i.; Chang, H.-C.; Takenobu, T.; Murayama, Y.; Kanbara, T.; Aoyama, T.; Sassa, T.; Wada, T.; Tanaka, D.; Kitagawa, S.; Iwasa, Y.; Akutagawa, T.; Nakamura, T. *J. Am. Chem. Soc.* **2005**, *127*, 10012−10013.
(24) Smith, A. G.; Tasker, P. A.; White, D. J. *Coord. Chem. Rev.* **2003**, *241*, 61−85.
(25) Tasker, P.; Gasperov, V. *Macrocyclic Chem.* **2005**, 365−382.
(26) Szymanowski, J. *Hydroxyoximes and Copper Hydrometallurgy*; CRC Press: Boca Raton, FL, 1993.
(27) *WIN-EPR Simfonia*, version 1.25; Bruker Analytische Messtechnik GmbH: Rheinstetten, Germany, 1996.
(28) Becke, A. D. *J. Chem. Phys.* **1993**, *98*, 5648−5652.
(29) Lee, C.; Yang, W.; Parr, R. G. *Phys. Rev. B* **1988**, *37*, 785−789.
(30) Ditchfield, R.; Hehre, W. J.; Pople, J. A. *J. Chem. Phys.* **1971**, *54*, 724−728.
(31) Frisch, M. J.; Trucks, G. W.; Schlegel, H. B.; Scuseria, G. E.; Robb, M. A.; Cheeseman, J. R.; J. A. Montgomery, J.; Vreven, T.; Kudin, K. N.; Burant, J. C.; Millam, J. M.; Iyengar, S. S.; Tomasi, J.; Barone, V.; Mennucci, B.; Cossi, M.; Scalmani, G.; Rega, N.; Petersson, G. A.; Nakatsuji, H.; Hada, M.; Ehara, M.; Toyota, K.; Fukuda, R.; Hasegawa, J.; Ishida, M.; Nakajima, T.; Honda, Y.; Kitao, O.; Nakai, H.; Klene, M.; Li, X.; Knox, J. E.; Hratchian, H. P.; Cross, J. B.; Bakken, V.; Adamo, C.; Jaramillo, J.; Gomperts, R.; Stratmann, R. E.; Yazyev, O.; Austin, A. J.; Cammi, R.; Pomelli, C.Ochterski, J. W.; Ayala, P. Y.; Morokuma, K.; Voth, G. A.; Salvador, P.; Dannenberg, J. J.; Zakrzewski, V. G.; Dapprich, S.; Daniels, A. D.; Strain, M. C.; Farkas, O.; Malick, D. K.; Rabuck, A. D.; Raghavachari, K.; Foresman, J. B.; Ortiz, J. V.; Cui, Q.; Baboul, A. G.; Clifford, S.; Cioslowski, J.; ; Stefanov, B. B.; Liu, G.; Liashenko, A.; Piskorz, P.; Komaromi, I.; Martin, R. L.; Fox, D. J.; Keith, T.; M. A. Al-Laham.; Peng, C. Y.; Nanayakkara, A.; Challacombe, M.; Gill, P. M. W.; Johnson, B.; Chen, W.; Wong, M. W.; Gonzalez, C.; Pople, J. A. *Gaussian 03*, Revision E.01; Gaussian Inc.: Wallingford, CT, 2004.
(32) Thompson, M. A. *ArgusLab 4.0.1*; Planaria Software LLC: Seattle, WA.
(33) Ramakrishnan, C.; Geetha, Y. *J. Chem. Sci.* **1990**, *102*, 481−496.
(34) Taylor, R.; Macrae, C. F. *Acta Crystallogr., Sect. B* **2001**, *57*, 815−827.

(35) Bruno, I. J.; Cole, J. C.; Edgington, P. R.; Kessler, M.; Macrae, C. F.; McCabe, P.; Pearson, J.; Taylor, R. *Acta Crystallogr., Sect. B* **2002**, *58*, 389−397.
(36) Macrae, C. F.; Edgington, P. R.; McCabe, P.; Pidcock, E.; Shields, G. P.; Taylor, R.; Towler, M.; van de Streek, J. *J. Appl. Crystallogr.* **2006**, *39*, 453−457.
(37) Macrae, C. F.; Bruno, I. J.; Chisholm, J. A.; Edgington, P. R.; McCabe, P.; Pidcock, E.; Rodriguez-Monge, L.; Taylor, R.; van de Streek, J.; Wood, P. A. *J. Appl. Crystallogr.* **2008**, *41*, 466−470.
(38) Marom, N.; Hod, O.; Scuseria, G. E.; Kronik, L. *J. Chem. Phys.* **2008**, *128*, 164107.
(39) Aristov, V. Y.; Molodtsova, O. V.; Maslyuk, V. V.; Vyalikh, D. V.; Zhilin, V. M.; Ossipyan, Y. A.; Bredow, T.; Mertig, I.; Knupfer, M. *J. Chem. Phys.* **2008**, *128*, 034703.
(40) King, E. R.; Betley, T. A. *J. Am. Chem. Soc.* **2009**, *131*, 14374−14380.
(41) Westcott, B. L.; Gruhn, N. E.; Michelsen, L. J.; Lichtenberger, D. L. *J. Am. Chem. Soc.* **2000**, *122*, 8083−8084.
(42) Basu, P. *J. Chem. Educ.* **2001**, *78*, 666.
(43) Calle, C.; Schweiger, A.; Mitrikas, G. *Inorg. Chem.* **2007**, *46*, 1847−1855.
(44) Marom, N.; Kronik, L. *Appl. Phys. A: Mater. Sci. Process.* **2009**, *95*, 159−163.
(45) Carlin, R. L. *Magnetochemistry*; Springer-Verlag : Berlin, Germany, 1986.
(46) Bonner, J. C.; Fisher, M. E. *Phys. Rev.* **1964**, *135*, A640.
(47) Estes, W. E.; Gavel, D. P.; Hatfield, W. E.; Hodgson, D. J. *Inorg. Chem.* **1978**, *17*, 1415−1421.
(48) Sung Hoon, K.; Sun Hee, L.; Jin, J. *IEEE Electron Device Lett.* **2010**, *31*, 1044−1046.
(49) Tello, M.; Chiesa, M.; Duffy, C. M.; Sirringhaus, H. *Adv. Funct. Mater.* **2008**, *18*, 3907−3913.